Electron charge dynamics and charge separation: A response theory approach

Lionel Lacombe[1,2] Lucia Reining[1,2] and Vitaly Gorelov[1,2⋆],

1 LSI, CNRS, CEA/DRF/IRAMIS, École Polytechnique, Institut Polytechnique de Paris, F-91120 Palaiseau, France
2 European Theoretical Spectroscopy Facility (ETSF)

⋆ vitaly.gorelov@polytechnique.edu

Abstract

This study applies response theory to investigate electron charge dynamics, with a particular focus on charge separation. We analytically assess the strengths and limitations of linear and quadratic response theories in describing charge density and current, illustrated by a model that simulates charge transfer systems. While linear response accurately captures optical properties, the quadratic response contains the minimal ingredients required to describe charge dynamics and separation. Notably, it closely matches exact time propagation results in some regime that we identify. We propose and test several approximations to the quadratic response and explore the influence of higher-order terms and the effect of on-site and nearest-neighbour interactions U and V.

Received Date
Accepted Date
Published Date

Contents

1 Introduction **2**

2 Theoretical framework **3**
2.1 Time propagation 3
2.2 Response theory 4
2.2.1 Linear response and its limitations 5
2.2.2 Quadratic response: analysis and limitations 6
2.3 Higher orders: what can they add? 9

3 The model **10**

4 Results and discussion **11**
4.1 Charge dynamics: linear and quadratic regime 12
4.2 Current vs. charge dynamics 13
4.3 Second order: limits and analyses 14
4.4 Second order: approximations 16
4.5 Interaction 17

5 Conclusions **18**

A Changing perturbation extension 19

B Scaling with system size 20

References 20

1 Introduction

Accurate modeling of electron charge dynamics is crucial for addressing a wide range of fundamental questions in physics and chemistry. Understanding the mechanisms of charge transfer and the separation of electrons and holes is a key challenge. These processes play a pivotal role in numerous technological applications, including photovoltaics, photocatalysis, and chemical reactions. For example, the efficient generation and transfer of charge carriers directly impacts the design and performance of solar cells, while charge separation dynamics are fundamental to catalyzing chemical transformations in many photo-activated processes.

To model these phenomena, various computational approaches have been developed, each with its own set of advantages and limitations. Among the most widely used techniques are Time-Dependent Density Functional Theory (TDDFT) [1,2] and Non-Equilibrium Green's Functions (NEGF) [3].

Real-time implementation of TDDFT to describe excited charge dynamics [4–6] is favored for its balance of computational efficiency and accuracy. However, it still struggles with incorporating many-body effects, since the exact exchange-correlation (xc) functional is unknown [7], and it is still computationally challenging to access long time scales. Current approximations to the xc functional cannot accurately describe the charge transfer, although a partial description of charge transfer is possible in generalized Kohn-Sham, for example using hybrid functionals [6,8]. There has been a recent progress, with a reformulation of TDDFT that uses response quantities for real time propagation [9].

Ab-initio calculations using NEGF are possible under the Generalised Kadanoff-Baym Ansatz [10]. This robust approximation offers a rigorous treatment of electron-electron and electron-phonon interactions at non-equilibrium conditions. Although it can scale linearly with propagation time [11], it remains computationally demanding and it is limited to short time scales, small systems, or parameterized model Hamiltonians [12–24].

A central challenge in modeling charge dynamics is the development of theoretical frameworks that remain accurate across time scales, perturbation strengths, and interaction regimes. This work explores a general response theory approach, including both linear [25] and quadratic [26] formulations, to compute time-dependent observables. Linear response is widely used for calculating ~~spectral~~ properties such as absorption and electron energy loss [27], while quadratic response captures nonlinear phenomena like second-harmonic generation [26,28]. Quadratic response also enables the study of nonlinear effects such as the electro-optic effect [29] and the shift current responsible for the bulk photovoltaic effect [30]. However they are rarely used to describe charge dynamics.

In practice, first- and second-order response functions are often computed within the independent-particle approximation, sometimes accounting for local field effects [31–34], and extended to include excitonic effects using the Bethe–Salpeter equation [13,35,36].

However, while response theory allows systematic inclusion of many-body effects and in principle enables access to very long simulation times, it remains perturbative and is valid near equilibrium. The goal of this work is to identify the regimes where linear and second-order

responses yield reliable results, both on the basis of general arguments and considering our particular case of charge separation in a small model.

This article will explore the following key questions on charge dynamics and response behavior: *How does charge dynamics differ in linear and quadratic response? Can charge dynamics and charge separation be accurately described within these two frameworks? What is the range of validity for linear and quadratic response in relation to perturbation amplitude, time- and length-scales? And finally, how does the Coulomb interaction influence these findings?*

The structure of the article is as follows. Section 2.1 introduces the exact time propagation from the ground state. Linear and quadratic response formalisms for time-dependent observables such as charge density and current are presented in Sec. 2.2, with higher-order contributions discussed in Sec. 2.3. A minimal site-based model, mimicking an optoelectronic device, is introduced in Sec. 3. The results are analyzed in Sec. 4, beginning with the validity of linear and quadratic regimes for charge density (Sec. 4.1) and current (Sec. 4.2). Section 4.3 provides an analysis of perturbation amplitude and the crossover from linear to higher-order regimes across observables, followed by Section 4.4 with practical approximations to second-order response. Section 4.5 demonstrates the effect of an onsite interaction U on the accuracy of the response approach. Conclusions are presented in Sec. 5.

2 Theoretical framework

2.1 Time propagation

We consider a system subject to a time-dependent perturbation added to a static Hamiltonian $\hat{H} + \hat{V}_{ext}(t)$, where the scalar potential $\hat{V}_{ext}(t) = \int d\mathbf{r}\hat{n}(\mathbf{r},t)V_{ext}(\mathbf{r},t)$ couples to the electron density operator $\hat{n}(\mathbf{r},t)$. Other types of external perturbations, such as vector electric or magnetic fields, would simply lead to modifications of the perturbation matrix elements (V_{IJ}, see Eq. 4). A many-body state $|\Psi(t)\rangle$ evolves in time as:

$$|\Psi(t)\rangle = \mathcal{T}\exp\left(-i[\hat{H}t + \int_{-\infty}^{t} dt'\hat{V}_{ext}(t')]\right)|\Psi_0\rangle, \tag{1}$$

where $|\Psi_0\rangle = |\Psi(t=0)\rangle$ and the evolution operator is the time-ordered exponential with $\mathcal{T}$ as the time-ordering operator [3]. We implement this expression by discretizing time into small time intervals, dt. At each time step s, the operator $\hat{H} + \hat{V}_{ext}(sdt)$ is diagonalized, such that $\hat{H} + \hat{V}_{ext}(sdt) = UDU^{-1}$, where $D(s)$ is the diagonal matrix of eigenvalues and $U(s)$ is the matrix of eigenvectors. The exponential operator can then be expressed as $e^{-idt(\hat{H}+\hat{V}_{ext}(sdt))} = Ue^{-idtD}U^{-1}$. Albeit restricted to small systems, this approach has the benefit of being easy to implement and the propagation remains unitary. With decreasing dt, the result converges to the exact solution.

The time evolution of observables, specifically, the electron density $\hat{O} \equiv \hat{n}(\mathbf{r})$ and current density $\hat{O} \equiv \hat{\mathbf{j}}(\mathbf{r})$, is analyzed in this work. Expanding the time-dependent wave function in the eigenstates of the unperturbed Hamiltonian, $\hat{H}$, $|\Psi(t)\rangle = \sum_I e^{-iE_I t}c_I(t)|\Psi_I\rangle$, a time-dependent observable $O(t)$ can be expressed as

$$O(t) = \langle\Psi(t)|\hat{O}|\Psi(t)\rangle = \sum_{IJ} e^{i\Delta_{IJ}t}c_I^*(t)c_J(t)O_{IJ} \equiv \sum_{IJ}\rho_{JI}(t)O_{IJ}, \tag{2}$$

where $\Delta_{IJ} = E_I - E_J$ denotes the energy difference between eigenstates, and $O_{IJ} = \langle\Psi_I|\hat{O}|\Psi_J\rangle$ is the matrix element of the observable, which governs the spatial structure of the charge dynamics. The many-body density matrix $\rho_{JI}(t) = e^{i\Delta_{IJ}t}c_I^*(t)c_J(t)$ encodes the quantum co-

herence of the time-dependent state $|\Psi(t)\rangle$ [26, 37]. The time-dependent coefficients $c_I(t)$ evolve according to

$$c_I(t) = \sum_J \left[\exp\left(-i \int_{-\infty}^{t} \hat{V}_{ext}(t')dt' \right) \right]_{IJ} c_J(0), \tag{3}$$

where evolution operator in interaction picture is the time ordered exponential. When the initial state is the ground state, $c_J(0) = c_0(0)\delta_{J0}$ and the sum over J disappears. The matrix elements of $\hat{V}_{ext}(t)$,

$$V_{IJ}(t) = e^{i\Delta_{IJ}t} \int d\mathbf{r} V_{ext}(\mathbf{r}, t) n_{IJ}(\mathbf{r}) \tag{4}$$

are non zero only when the state I and state J have a non-vanishing spatial overlap between each other and with the perturbation $V_{ext}(\mathbf{r}, t)$.

2.2 Response theory

Response theory is obtained by expanding the time-ordered exponential in Eq. 3 in powers of the perturbation $\hat{V}_{ext}(t)$. This expansion breaks unitarity, leading to a violation of wavefunction normalization; truncating at n-th order introduces errors of order $n+1$ in the perturbation strength. Applying this expansion to the time-dependent density matrix yields $\rho_{IJ}(t) = \sum_{n=0}^{\infty} \rho_{IJ}^{(n)}(t)$. The general form of the response theory involves time-ordered nested commutators of the perturbation with the unperturbed Hamiltonian,

$$\rho_{IJ}^{(n)}(t) = e^{-i\Delta_{IJ}t}(-i)^n \int_{-\infty}^{t} dt_1 ... \int_{-\infty}^{t_{n-1}} dt_n [\hat{V}_{ext}(t_1), [\hat{V}_{ext}(t_2) ..., [\hat{V}_{ext}(t_n), \hat{\rho}^{(0)}] ...]]_{IJ}. \tag{5}$$

Starting from the ground state, the zeroth order density matrix is $\rho_{IJ}^{(0)} = \delta_{I0}\delta_{J0}$.

Traditionally, the system's response to external perturbations is expressed in terms of response functions [25, 38]. Up to second order, the change in the expectation value of an observable $\hat{O}$, defined as $\delta\langle\hat{O}(t)\rangle = \langle\hat{O}(t)\rangle - \langle\hat{O}(0)\rangle$, induced from the ground state by a scalar external potential $V_{ext}(\mathbf{r}, t)$, can be written in terms of the corresponding linear and nonlinear response functions.

$$\begin{aligned} \delta\langle\hat{O}(\mathbf{r}, t)\rangle = & \int d\mathbf{r}_1 dt_1 \chi_{\hat{O}}^{(1)}(\mathbf{r}, \mathbf{r}_1, t - t_1) V_{ext}(\mathbf{r}_1, t_1) \\ & + \int d\mathbf{r}_1 dt_1 d\mathbf{r}_2 dt_2 \chi_{\hat{O}}^{(2)}(\mathbf{r}, \mathbf{r}_1, \mathbf{r}_2, t - t_1, t - t_2) V_{ext}(\mathbf{r}_1, t_1) V_{ext}(\mathbf{r}_2, t_2) + ... \end{aligned} \tag{6}$$

Throughout this article we will focus on space dependent observables, such as charge and current densities, since we are interested in charge dynamics and separation. The first $\chi_{\hat{O}}^{(1)}$ and the second $\chi_{\hat{O}}^{(2)}$ order response functions are the response of an observable $\hat{O}$ to an external potential $V_{ext}(\mathbf{r}, t)$.

One key strength of response theory is its ability to efficiently incorporate interactions, including excitons via the Bethe–Salpeter equation [27] and electron–phonon or plasmon couplings through, for example, cumulant expansions [39, 40].

Moreover, unlike exact time propagation, which requires re-solving the full dynamics for each perturbation, response functions can be computed once to be reused later for different

perturbations. This facilitates efficient evaluation of system responses to arbitrary perturbations, time profiles, and field strengths, of course within the limits of validity of perturbation theory.

In practice, response functions are often approximated to reduce computational complexity. Common approaches include the random phase approximation (RPA), time-dependent Hartree-Fock (TDHF) and approximations to time-dependent Green's function functional theory (TDGFFT), such as time-dependent GW (TDGW) [41], and approximations to time-dependent density functional theory (TDDFT) [1, 27]. These methods introduce varying degrees of approximation to the exchange and correlation effects. In this work, the focus is on the exact expressions for the response functions, derived directly from the time-dependent many-body wavefunction, to provide a benchmark for assessing the accuracy of response theories, and we will mostly look at the non-interacting problem.

2.2.1 Linear response and its limitations

The analysis begins with the dynamics obtained from linear response, which follows from Eq. 5 with $n = 1$. Throughout, only systems with real-valued wavefunctions Ψ_I are considered. In that case, the linear response function for any time- and space- dependent observable $\hat{O}(\mathbf{r}, t)$, $\chi^{(1)}_{\hat{O}}$, can be expressed as

$$\chi^{(1)}_{\hat{O}}(\mathbf{r}, \mathbf{r}_1; t - t_1) = -2\theta(t - t_1) \sum_I O_{0I}(\mathbf{r}) n_{I0}(\mathbf{r}_1) A^{n/j}[\Delta_{I0}(t - t_1)] \tag{7}$$

where $\theta(t)$ is a Heaviside step function, $O_{IJ}(\mathbf{r}) = \langle \Psi_I | \hat{O}(\mathbf{r}) | \Psi_J \rangle$, $A^n[\cdot] \equiv \sin[\cdot]$ for a real observable, for which $\hat{O}^* = \hat{O}$, and $A^j[\cdot] \equiv i\cos[\cdot]$ for an imaginary observable operator, for which $\hat{O}^* = -\hat{O}$. Assuming that the external perturbation can be factorized into spatial and temporal components $V_{ext}(\mathbf{r}, t) = u(\mathbf{r})e(t)$, the first order response reads

$$\delta O^{(1)}(\mathbf{r}, t) = -2 \sum_I O_{0I}(\mathbf{r}) \tilde{V}_{I0} \int_{-\infty}^{t} dt_1 A^{n/j}[\Delta_{I0}(t - t_1)] e(t_1), \tag{8}$$

where $\tilde{V}_{IJ} = \int d\mathbf{r}_1 u(\mathbf{r}_1) n_{IJ}(\mathbf{r}_1)$ is the spatial overlap of the states with the perturbation.

Comparison of Eq. 8 with the exact time propagation in Eq. 2 reveals that first-order response lacks terms involving excited-state couplings, $O_{IJ}(\mathbf{r})$ for $I, J \neq 0$. Since it depends only on the overlap between the ground state, an excited state and the perturbation, the linear response is not able to have a non-vanishing value beyond the spatial extension of the ground state (see Fig. 1(a) for illustration), unless the observable operator is non-local.

This means that, when the ground state is mostly localised in the region where the perturbation is applied, a charge transfer is only possible between the states overlapping with the ground state (see Fig. 1(a) for illustration). The response at distances far from the localisation of the ground state cannot be observed. The current operator involves the gradient, which is not purely local operator, and results in a slightly more delocalized expectation value than the charge density. Therefore, it favours a slightly better linear response result in the region where the ground state has very low amplitude. This will be further illustrated in Section 4.

The time-dependent contribution to the response changes depending on the observable. For a real observable, such as the induced charge density $\delta n(\mathbf{r}, t)$, and a local, instantaneous perturbation of the form $V_{ext}(\mathbf{r}, t) = u(\mathbf{r})\delta(t)$, the time-dependent part of Eq. 8 becomes

$$\theta(t) \int_{-\infty}^{t} dt_1 A^n[\Delta_{I0}(t - t_1)] \delta(t_1) = \theta(t) \sin[\Delta_{I0} t]. \tag{9}$$

The response is governed by oscillations at frequencies corresponding to energy differences Δ_{I0}.

In the case of an oscillating perturbation in time, $V_{ext}(\mathbf{r},t) = u(\mathbf{r})\theta(t)\sin(\omega t)$, the corresponding contribution to the linear induced charge density becomes

$$\theta(t)\int_{-\infty}^{t} dt_1 A^n[\Delta_{I0}(t-t_1)]\theta(t_1)\sin(\omega t_1) = \theta(t)\frac{\Delta_{I0}\sin[\omega t]-\omega\sin[\Delta_{I0}t]}{\Delta_{I0}^2-\omega^2}. \tag{10}$$

At resonance, where $\Delta_{I0}=\omega$, the charge propagation oscillates as $(\sin[\omega t]-\omega t\cos[\omega t])/2\omega$.

Charge separation can be intuitively understood as the condition where the induced density increases on one side of the system and decreases on the other. For positive induced density one can define the electron propagation and for negative, the hole propagation.

For both perturbations, charge separation can only occur on time scales shorter than $t<\pi/\Delta_{I0}$ (if $\omega>\Delta_{I0}$ for oscillating perturbation, otherwise shorter than $t<\pi/\omega$), and can never be longer than the inverse of the gap, past this time, the charge density is changing sign. For both considered perturbations, the induced charge would always oscillate around zero in every point in space, indicating that there is no possibility to see a net charge separation in linear response (see section 4.1 for an illustration).

Considering now an imaginary operator, such as the current-density for which $\hat{\mathbf{j}}^*(\mathbf{r}) = -\hat{\mathbf{j}}(\mathbf{r})$. In the case of an instantaneous perturbation, the current density can be obtained by replacing $\sin[\Delta_{I0}t]$ by $i\cos[\Delta_{I0}t]$ in Eq. 9. For a real valued wavefunction $\mathbf{j}_{00}(\mathbf{r})=0$, meaning that the time average of linear response current is zero, no DC component is present.

In the case of an oscillating perturbation, $e(t)=\theta(t)\sin(\omega t)$, the resulting time-dependent part of the current density is given by

$$\theta(t)\int_{-\infty}^{t} dt_1 A^j[\Delta_{I0}(t-t_1)]\theta(t_1)\sin(\omega t_1) = \theta(t)i\frac{2\Delta_{I0}(\cos[\Delta_{I0}t]-\cos[\omega t])}{\omega^2-\Delta_{I0}^2}. \tag{11}$$

At the resonance $\Delta_{I0}=\omega$ the time dependency is governed by $t\sin(\omega t)$. A crucial condition for observing net charge transport is the presence of a nonzero DC component in the current, i.e., a finite time-averaged value $\langle\mathbf{j}(\mathbf{r},t)\rangle_t \neq 0$. Such a contribution is absent in the non-resonant linear response regime, where the current oscillates symmetrically around zero. However, averaging the time-dependent part over a period of oscillations, $T=2\pi/\omega$, at the resonance results in $2\pi/\omega^2$ and, depending on the corresponding matrix elements in Eq. 8, might be non-vanishing resulting in a finite DC component.

For both considered perturbations and observables, the ground state doesn't contribute to the summation in Eq. 8, as $\Delta_{00}=0$ and $\mathbf{j}_{00}(\mathbf{r})=0$. Any linear combination of perturbations leads to a corresponding linear superposition of the individual linear responses.

2.2.2 Quadratic response: analysis and limitations

Charge separation and propagation beyond the region of localization of the ground state requires the quadratic response $\chi^{(2)}$, defined as:

$$\begin{aligned}\chi^{(2)}_{\hat{O}}(\mathbf{r},\mathbf{r}_1,\mathbf{r}_2,t,t_1,t_2) = \quad & -2\theta(t-t_1)\theta(t-t_2)\theta(t_1-t_2)\sum_{IJ} \\ & \Big[O_{0I}(\mathbf{r})n_{IJ}(\mathbf{r}_1)n_{J0}(\mathbf{r}_2)A^{n/j}[\Delta_{I0}t+\Delta_{JI}t_1+\Delta_{0J}t_2] \\ & -O_{IJ}(\mathbf{r})n_{0I}(\mathbf{r}_1)n_{J0}(\mathbf{r}_2)A^{n/j}[\Delta_{I0}t_1+\Delta_{JI}t+\Delta_{0J}t_2]\Big],\end{aligned} \tag{12}$$

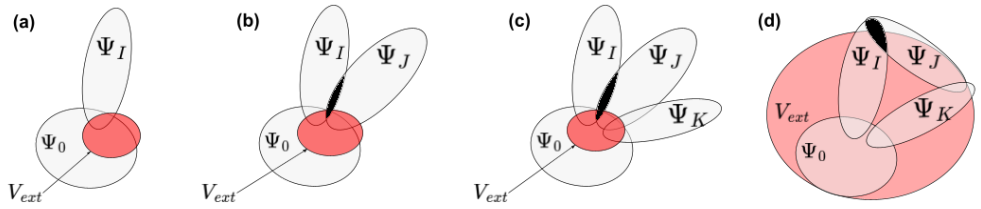

Figure 1: Schematic illustration of spatial overlaps between the excited states Ψ_I, the external perturbation V_{ext} and the ground state Ψ_0 that contribute in response theory up to the first order (a) (see Eqs. 8,20), second order (b) (see Eqs. 13,21) and third order (c), (d) (see Eq. 22) for only one element O_{IJ} of the sum in Eq. 2. (c) for a localized perturbation in third order (d) for a delocalized perturbation in third order. Black shade is the region, where the observable matrix element O_{IJ} can be non-zero .

where $A^n[\cdot] \equiv \sin[\cdot]$ for a real observable and $A^j[\cdot] \equiv i\cos[\cdot]$ for an imaginary observable operator. A second order contribution to an observable $\hat{O}$ in response to a generic perturbation is

$$\begin{aligned}\delta O^{(2)}(\mathbf{r},t) &= 2\sum_{J\neq 0}(O_{00}(\mathbf{r})-O_{JJ}(\mathbf{r}))\tilde{V}_{0J}^2 B_{0J}^{'n/j}(t) \\ &-2\sum_{I>J,J\neq 0} O_{IJ}(\mathbf{r})\tilde{V}_{0I}\tilde{V}_{J0}B_{IJ}^{''n/j}(t) \\ &+2\sum_{I\neq 0,J\neq 0} O_{0I}(\mathbf{r})\tilde{V}_{IJ}\tilde{V}_{J0}B_{IJ}^{'n/j}(t), \end{aligned} \tag{13}$$

where the terms have been regrouped by their importance for charge dynamics. The first term is the dominant one. It comes from expanding the time-dependent wavefunctions (or coefficients) up to the first order of Eq. 2, only keeping the diagonal contributions, and it is determined by the excited state expectation values of the observable. These quantities can be obtained from linear response TDDFT [42, 43]. The second term, arising from transitions between excited states, originates from the second-order expansion of the time-dependent wavefunctions in Eq. 2. The third term, in the case when $O_{0I}(\mathbf{r}) \approx 0$ outside the ground state localization, contributes little to the second-order response, this is the linear-response-like term. Unlike the linear response, the first two terms in the second-order contribution involve the full set of matrix elements $O_{IJ}(\mathbf{r})$, qualitatively they contain all the information of the exact time-propagation expression in Eq. 2. Relying on the excited states overlaps, the second order is able to propagate charge beyond the extension of the ground state, see the black shade on Fig. 1(b). However, the overlap between an excited state, the ground state and the perturbation, $\tilde{V}_{0I}$, has to be non-zero.

Evaluating Eq. 13 requires computing the overlap integrals $\tilde{V}_{IJ}$, which can be performed in advance. Importantly, only the elements involving the ground state of the $\tilde{V}_{IJ}$ matrix enter the first two terms of Eqs. 13. Considering the symmetry of the spatial part of the second term in Eq. 13 with respect to the exchange of I and J, the sum is reduced to only terms with $I > J$. The temporal dependence is governed by the factors $B^{'}$ and $B^{''}$.

In the case of the second order induced charge density $\delta n(\mathbf{r},t)$ for the instantaneous perturbation in time, $V_{ext}(\mathbf{r},t) = u(\mathbf{r})\delta(t)$, the time-dependent parts $B_{IJ}^{'n}(t)$ and $B_{IJ}^{''n}(t)$ become:

$$\begin{aligned} B_{IJ}^{'n}(t) &= \theta(t)\int_0^t dt_1\int_0^{t_1} dt_2 \cos[\Delta_{I0}t + \Delta_{JI}t_1 + \Delta_{0J}t_2]\,\delta(t_1)\delta(t_2) = \theta(t)\cos[\Delta_{I0}(t)], \\ B_{IJ}^{''n}(t) &= \theta(t)\int_0^t dt_1\int_0^{t_1} dt_2 \cos[\Delta_{I0}t_1 + \Delta_{JI}t + \Delta_{0J}t_2]\,\delta(t_1)\delta(t_2) = \theta(t)2\cos[\Delta_{JI}(t)], \end{aligned} \tag{14}$$

which results in $B^{'n}_{0J}(t) = \theta(t)$. This gives a constant offset to the charge dynamics necessary to the charge separation.

Considering further an oscillating time dependent part of the external potential, $V_{ext}(\mathbf{r},t) = u(\mathbf{r})\theta(t)\sin(\omega t)$, the second order time integrals become:

$$\begin{aligned} B^{'n}_{IJ}(t) &= \theta(t)\int_0^t dt_1 \int_0^{t_1} dt_2 \cos[\Delta_{I0}t + \Delta_{JI}t_1 + \Delta_{0J}t_2]\sin(\omega t_1)\sin(\omega t_2) = \\ &= \frac{\theta(t)}{2(\Delta^2_{J0}-\omega^2)}\Big(\frac{2\omega^2\cos[\Delta_{I0}t] + \omega(\Delta_{JI}-\omega)\cos[(\Delta_{J0}+\omega)t] - \omega(\Delta_{JI}+\omega)\cos[(\Delta_{J0}-\omega)t]}{(\Delta^2_{JI}-\omega^2)} \\ &\quad -\frac{\Delta_{0J}}{\Delta_{I0}}(\cos[\Delta_{I0}t]-1) + \frac{(\Delta_{J0}\Delta_{I0}+2\omega^2)(\cos[2\omega t]-\cos[\Delta_{I0}t])}{(\Delta^2_{I0}-4\omega^2)}\Big), \end{aligned} \tag{15}$$

$$B^{'n}_{0J}(t) = \theta(t)\Big[\frac{(1-\cos[2\omega t])}{4(\Delta^2_{J0}-\omega^2)} + \frac{2\omega^2 + \omega(\Delta_{J0}-\omega)\cos[(\Delta_{J0}+\omega)t] - \omega(\Delta_{J0}+\omega)\cos[(\Delta_{J0}-\omega)t]}{2(\Delta^2_{J0}-\omega^2)^2}\Big], \tag{16}$$

$$\begin{aligned} B^{''n}_{IJ}(t) &= \frac{\theta(t)}{2(\Delta^2_{J0}-\omega^2)(\Delta^2_{I0}-\omega^2)}\Big(2\omega^2\cos[\Delta_{IJ}t] + (\Delta_{J0}\Delta_{I0}+\omega^2) - (\Delta_{J0}\Delta_{I0}-\omega^2)\cos[2\omega t] \\ &\quad -\omega(\Delta_{I0}+\omega)\cos[(\Delta_{J0}-\omega)t] - \omega(\Delta_{J0}+\omega)\cos[(\Delta_{I0}-\omega)t] \\ &\quad +\omega(\Delta_{I0}-\omega)\cos[(\Delta_{J0}+\omega)t] + \omega(\Delta_{J0}-\omega)\cos[(\Delta_{I0}+\omega)t]\Big). \end{aligned} \tag{17}$$

In $B^{'n}_{IJ}(t)$ the resonance is reached when either ω or 2ω match the transition energies. The $B^{''n}_{IJ}(t)$ term is resonant only when the transition energies match ω. The time dependence of the second-order response features oscillations at frequencies determined by the transition energies Δ_{IJ}, the perturbation frequency ω and 2ω, as well as their sums and differences. Beyond the oscillatory behavior, a key contribution arises from the constant offset in $B^{'n}_{0J}(t)$, which ensures that the induced density vanishes at $t = 0$. This term shifts the dynamics to enable charge separation (see Sec. 4). At resonance conditions $\Delta_{J0/I0} \pm \omega = 0$, the second order response diverges faster than the first order (due to the $1/(\Delta^2_{J0}-\omega^2)^2$ in $B^{'n}_{0J}(t)$), indicating a breakdown of the response theory. Additional resonances occur when $\Delta_{I0} \pm 2\omega = 0$, but these are less significant far from the ground-state region, since it only enters the third term of Eq. 13.

In the second order current-density response, for real valued wavefunctions $\mathbf{j}_{II}(\mathbf{r}) = 0$, the first term in Eq. 13 disappears. For an instantaneous delta-function perturbation, the current density follows from Eq. 14 by replacing $\cos[\Delta_{JI/I0}t]$ with $i\sin[\Delta_{JI/I0}t]$. In the case of an oscillating perturbation, the corresponding expression for the current density time integrals that enter Eq. 13 read:

$$\begin{aligned} B^{'j}_{IJ}(t) &= \frac{\theta(t)}{2(\Delta^2_{J0}-\omega^2)}\Big(\frac{2\omega^2\sin[\Delta_{I0}t] + \omega(\Delta_{JI}-\omega)\sin[(\Delta_{J0}+\omega)t] - \omega(\Delta_{JI}+\omega)\sin[(\Delta_{J0}-\omega)t]}{(\Delta^2_{JI}-\omega^2)} - \\ &\quad -\frac{\Delta_{0J}}{\Delta_{I0}}\sin[\Delta_{I0}t] - \frac{(\Delta_{J0}\Delta_{I0}+2\omega^2)\sin[\Delta_{I0}t] - 2\omega(\Delta_{I0}+2\Delta_{J0})\sin[2\omega t]}{(\Delta^2_{I0}-4\omega^2)}\Big), \end{aligned} \tag{18}$$

$$\begin{aligned} B^{''j}_{IJ}(t) &= \frac{\theta(t)}{2(\Delta^2_{J0}-\omega^2)(\Delta^2_{I0}-\omega^2)}\Big(2\omega\Delta_{JI}\sin[2\omega t] + 2\omega^2\sin[\Delta_{JI}t] + \\ &\quad +\omega(\Delta_{I0}-\omega)\sin[(\Delta_{J0}+\omega)t] - \omega(\Delta_{I0}+\omega)\sin[(\Delta_{J0}-\omega)t] - \\ &\quad -\omega(\Delta_{J0}-\omega)\sin[(\Delta_{I0}+\omega)t] + \omega(\Delta_{J0}+\omega)\sin[(\Delta_{I0}-\omega)t]\Big). \end{aligned} \tag{19}$$

For an oscillating perturbation a non-vanishing DC component in the current emerges at resonance due to the terms like $\lim_{\Delta_{J0}\to\pm\omega} \frac{\sin[(\Delta_{J0}\pm\omega)t]}{(\Delta_{J0}\pm\omega)} = t$. In the case of a perturbation by a vector potential, this effect corresponds to the generation of a shift current, also known as the bulk photovoltaic effect (BPVE), as discussed in Refs. [44, 45]. This mechanism enables net current flow in the absence of external bias and plays a central role in nonlinear optical and transport phenomena.

In the linear and quadratic response, for an oscillating perturbation, a convergence parameter can be identified from Eqs. 10 and 11 in linear and Eqs. 15-19 in quadratic response, $I/(\Delta_{J0} \pm \omega)$, where I is the perturbation amplitude. The response theory breaks down if I is large or if the resonance is reached $\Delta_{J0} = \pm\omega$.

2.3 Higher orders: what can they add?

To understand the contributions of higher orders, it is useful to look at the density matrix expansion defined in Eq. 5 and the corresponding overlaps between the states. The focus here will be on propagating the charge far from the ground state and from the perturbation.

The main contributions to the density matrix in first order are coming from one of the elements of the commutator:

$$\rho^{(1)}_{IJ}(t) \propto \tilde{V}_{0I} B_{IJ}(t) \delta_{0J}. \tag{20}$$

In linear response, only off-diagonal elements of the density matrix contribute, while diagonal terms such as $\rho^{(0)}_{00}$ vanish. As a result, net charge transport requires the inclusion of higher-order processes. In the second-order response, all matrix elements can contribute, since relevant terms in the commutator of Eq. 5 are not restricted by δ_{0J}, enabling asymmetry and transport in the induced dynamics. One of the elements of the second order of Eq. 5 is

$$\rho^{(2)}_{IJ}(t) \propto \tilde{V}_{0I} \tilde{V}_{J0} B_{IJ}(t). \tag{21}$$

The condition for a nonzero second-order contribution is a finite overlap between the excited states I and J that enters the observable O_{IJ} in Eq. 2, the ground state, and the applied perturbation. Similarly, the third-order (and higher-order) response generate the full set of density matrix elements, e.g.

$$\rho^{(3)}_{IJ}(t) \propto \sum_K \tilde{V}_{0I} \tilde{V}_{JK} \tilde{V}_{K0} B_{IJK}(t). \tag{22}$$

In this expression, contrary to the second order, not all the excited states (e.g. J) must overlap with the ground state. Instead there is an extra overlap between states K and J and the perturbation and K must overlap with the ground state.

Consider two scenarios: first, when the perturbation is localized in the region of the ground state, which is illustrated in Fig. 1(c). In this case, the third-order response behaves similarly to the second-order response in terms of charge propagation. Shaded in black area is the overlap between the states I and J that contributes to an observable of interests, $O_{IJ}(\mathbf{r})$ (see Eq. 2). This area is the same in second, third and higher orders, meaning that the third (and higher) order response cannot propagate charge significantly further than the second order for a localized perturbation due to the persistent presence of the $\tilde{V}_{0I}$ terms across all orders.

In the second scenario, involving a fully delocalized perturbation (Fig. 1(d)), charge transport can extend beyond the range achievable in the second order. Here, when state J overlaps with K, which in turn overlaps with the ground state, there is a potential for charge to propagate further (black shaded area) that is not accessible by second order (see Appendix A).

For the fourth and higher orders, the situation remains similar. For a perturbation localized within the ground state, the requirement remains that all states must overlap with the ground state. The only quantitative change will be added from more elements like $\tilde{V}_{KL}$. In the case of a completely delocalized perturbation, higher-order responses allow for further charge propagation through sequential overlaps between the states, i.e. there will be additional elements added into the chain, e.g. Ψ_0 - Ψ_I - Ψ_J - Ψ_K - Ψ_0. However, of course, for a weak perturbation, these contributions will be smaller than in the second order.

3 The model

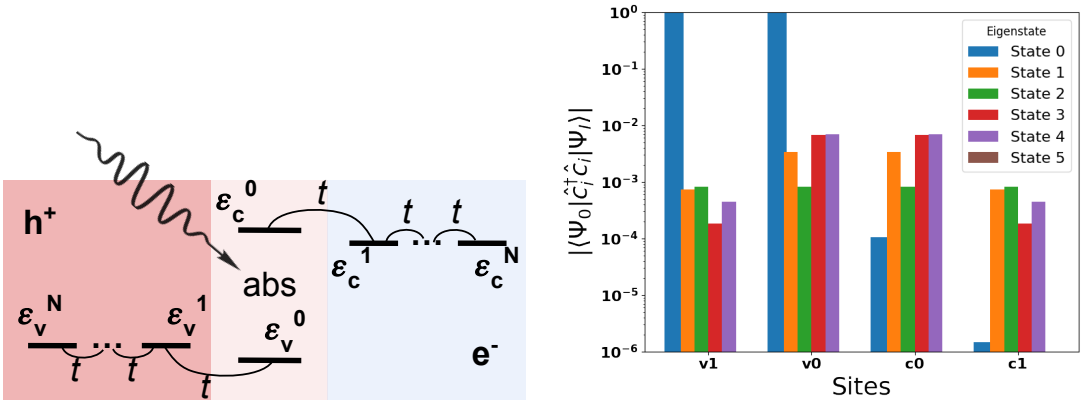

Figure 2: Left: Site model used in this work. The model is divided into three regions: absorber in the middle, electron transport layer (blue) and hole transport layer (red). $N+1$ electrons occupy lower energy (valence) sites vi connected with the hopping $t_h = 1$. The $N+1$ higher energy (conduction) sites ci, connected by a hopping $t_h = 1$ are separated by a single site energy $\epsilon_c^0 - \epsilon_v^0 = 10t_h$ in the absorber. The external field arrives in the absorber region. Right: matrix element $\langle\Psi_0|\hat{c}_i^\dagger\hat{c}_i|\Psi_I\rangle$ between the ground and excited states for $t_a = 0.1t_h$ projected onto the sites for a system with two valence and two conduction sites. State 5 doesn't have an overlap with the ground State 0.

To illustrate this discussion and to get further insight, we will use a model that simulates systems with interfaces where an external perturbation excites a charge in one region or material, after which the excited charge propagates into another region or material. This model aims to demonstrate charge separation into electrons and holes, a process prevalent in optoelectronics and particularly in photovoltaic systems. The choice of the model has to be a minimal yet comprehensive testbed for response theory in charge transfer. It should provide discrete eigenstates (we are working with finite systems), controllable energy offsets and explicit control over the matrix-element overlaps that couple the ground state to excited states (cf. $\tilde{V}_{0I}$ in Secs. 2.2-2.3). This setting contains the ingredients needed to diagnose when linear vs. quadratic response suffices for charge dynamics and separation, while keeping the analysis transparent. Our focus here is not on reproducing device-level numbers, but on establishing qualitative mechanisms and regimes of validity. We emphasize that infinite and semi-infinite systems as well as 2D and 3D dimensional interfaces are outside our present scope. We expect the semi-infinite leads to adjust spectral densities and long-time tails, that would change numbers and parameters of validity and would increase the period of oscillations to infinity. Increasing the dimensionality will allow a more realistic study of the charge dynamics, where the charge can move in the interface plane. However, the qualitative overlap-based conclusions we draw about the order of response needed for transport will hold. We leave the extensions

with realistic electrodes and environments to future work.

Our Hubbard-like model consists of $N+1$ lower energy sites and $N+1$ higher energy sites and a number of electrons $N_e = N+1$. The illustration of the model and the extension of the ground state can be found in Fig. 2.

$$\hat{H} = \sum_{i=0}^{N} \epsilon_v^i \hat{c}_{vi}^\dagger \hat{c}_{vi} + \sum_{i=0}^{N} \epsilon_c^i \hat{c}_{ci}^\dagger \hat{c}_{ci} - \sum_{i=0}^{N-1} t_h (\hat{c}_{vi}^\dagger \hat{c}_{vi+1} + \hat{c}_{vi+1}^\dagger \hat{c}_{vi}) - \sum_{i=0}^{N-1} t_h (\hat{c}_{ci}^\dagger \hat{c}_{ci+1} + \hat{c}_{ci+1}^\dagger \hat{c}_{ci}) + t_a (\hat{c}_{v0}^\dagger \hat{c}_{c0} + \hat{c}_{c0}^\dagger \hat{c}_{v0}), \tag{23}$$

were $\hat{c}_{\alpha i}$ ($\hat{c}_{\alpha i}^\dagger$) annihilates (creates) a fermion on site $i = 0, \ldots, N$ of side $\alpha \in \{v, c\}$. The on-site energies are ϵ_α^i; t_h is the nearest-neighbor hopping amplitude; t_a is a local hybridization between v and c at $i = 0$. The first lower energy site $v0$ and the first higher energy site $c0$ will represent the region, where the external perturbation acts. This region is called absorber. The rest of the low energy sites represent the hole transport layer and the rest of the high energy sites - the electron transport layer. In the following we choose the hopping between the $v0$ and $c0$ sites, $t_a < t_h$, such that, the $N_e = N+1$ electrons in the many-body ground state will mostly occupy $N+1$ lower sites, vi, and have a little occupation of higher energy sites, ci (see the blue column in the right panel of Fig. 2 for a system with 4 sites). Therefore will can call the lower energy sites - valence sites and higher energy sites - conduction sites. No spin is included, except in the last section 4.5.

For most of the discussion below we consider 2 valence and 2 conduction sites (unless it is stated otherwise). The characteristic energy difference in our system between conduction and valence sites is $\epsilon_c^0 - \epsilon_v^0 = 10 t_h$. The energy difference between the absorber region and electron/hole transport layer is $\epsilon_{v/c}^1 - \epsilon_{v/c}^0 = 1 t_h$. Except for the validity limits of response theory, the overall conclusions do not depend on the particular parameters.

The external perturbation acts only in the absorber region and is defined as $\hat{V}_{ext}^{ij}(t) = I \delta_{ic0} \delta_{jv0} (\hat{c}_{c0}^\dagger \hat{c}_{v0} + \hat{c}_{v0}^\dagger \hat{c}_{c0}) e(t)$. We have chosen such perturbation in order to study the dynamics far from it. We have verified that a delocalized perturbation that acts on the whole model doesn't change the main conclusions about the validity of the second order response theory. In both first- and second-order responses, the dominant terms involve $\tilde{V}_{0I}$, it contains the overlaps between excited states and the ground state (see Eq.8 and first two terms of Eq.13). Figure 2 (right panel) shows $\langle \Psi_0 | \hat{c}_i^\dagger \hat{c}_i | \Psi_I \rangle$ for $t_a = 0.1 t_h$, revealing nearly an order-of-magnitude larger overlap at absorption sites ($v0$, $c0$) than in the transport layers ($v1$, $c1$). Extending the perturbation to other sites thus has negligible impact on $\tilde{V}_{0I}$ (see Appendix A). The strength of the perturbation I and the perturbation frequency ω are the parameters that differentiate between different response regimes.

Consider a natural electric field scale in the Hubbard model as a field that does work comparable to a hopping $t_h \sim 1$ eV over a distance a: $E_0 \sim \frac{t_h}{ea} = 10^{10}$ V/m, where $a = 1$ and e - an electric charge. A solar intensity on a clear day can be assumed to be $I_s \approx 1000$ W/m^2 [46], converting it into an electric field intensity makes $E_s \sim 10^6$ V/m, which in the Hubbard model translates to $I \sim 10^{-4} t_h$. This is a very weak field, compared to a typical pump-probe experiment, where a pump probe $I \sim (0.1-1) t_h$ [47,48]. In fact, as can be seen in the next section, at $I \sim 10^{-4} t_h$ one can already observe some second order effect on charge dynamics.

4 Results and discussion

Here, the focus is on the excited charge dynamics within the presented model via examining the induced density and current. For the site model, this simplifies to the dynamics of a change on a site occupation number, $\delta n_{ii}(t)$, and the current between two sites $\delta j_{ii+1}(t)$ with respect to the

ground state. Our objective is to achieve charge separation, where electrons are transported to the electron transport layer, i.e. positive $\delta n_{ii}(t)$, and holes to the hole transport layer, i.e. negative $\delta n_{ii}(t)$. This should also result in a net DC current, i.e. $\langle j_{ii+1}(t)\rangle_t \neq 0$.

In the following the difference between the exact time propagation defined in Section 2.1 and the linear and quadratic response theory will be examined.

4.1 Charge dynamics: linear and quadratic regime

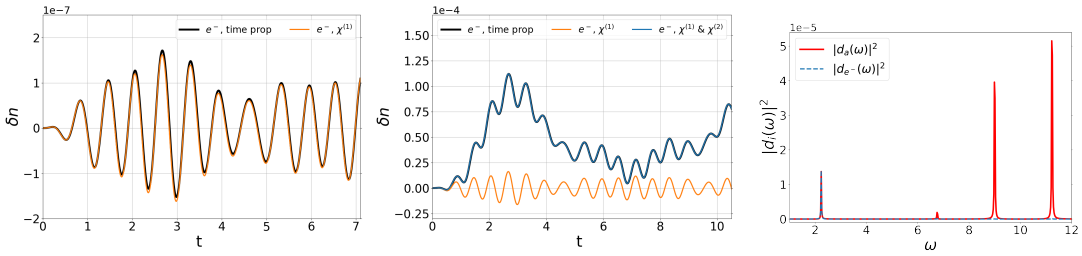

Figure 3: Left and Middle: Density of electron transport layers induced by an oscillating perturbation (for hole transport layer, the density is identical with a minus sign) for a system of two valence and two conduction sites. Orange lines indicate the linear response contribution. Blue lines - combined linear and quadratic contributions and black lines - exact dynamics. Left: $e(t) = 10^{-4} t_h \cdot \theta(t)\sin(\omega t)$ Middle: $e(t) = 10^{-2} t_h \cdot \theta(t)\sin(\omega t)$. Right: delta-kick perturbation $e(t) = \delta(t)$. Fourier transform of the dipole moment on the absorbtion site $c0$ (red) and on the electron transport layer $c1$ (blue).

Introducing the hopping $t_a \neq 0$ between the valence and conduction sites, e.g. between site $v0$ and $c0$, the ground state will have contributions from the conduction sites ci. Consequently, the matrix element entering the linear response, $n^i_{0I} \equiv \langle\Psi_0|\hat{c}^\dagger_i \hat{c}_i|\Psi_I\rangle \neq 0$, will be non-zero (right panel of Fig. 2). This results in a non-vanishing linear response contribution, as illustrated by the orange curves in Fig. 3 (left and middle panels). ~~Here and throughout the manuscript, the solid lines indicate the charge at electron transport layer and the dashed line the charge at hole transport layer.~~ The density of the hole transport layer is identical to the electron transport layer with a minus sign

In this subsection the perturbation frequency is $\omega = 10 t_h$, which is not resonant. For small enough perturbation $I \leq 10^{-4} t_h$ (Fig. 3 left), the charge dynamics is predominantly governed by the linear response regime. The linear response (orange lines) closely matches the exact dynamics (black line) over extended simulation periods. Only small differences between the linear response and exact dynamics are observed.

For perturbations strong enough to separate electrons and holes, $I > 10^{-4} t_h$ (see Fig. 3 middle panel), the linear response induced charge (orange lines) oscillates around zero, as indicated by the time dependency part of Eq. 10. The separation of charge occurs, when the induced density is positive on the electron transport layer (solid lines) and negative on the hole transport layer (dashed lines). The linear response alone always oscillates between positive and negative values and fails to separate charges for any perturbation strength. Including the second order response (blue lines) function $\chi^{(2)}$ recovers completely the charge dynamics.

For a non-resonant perturbation frequency, no deviation from exact dynamics is observed for any simulation time, which can be explained by the oscillating nature of the response. In fact, according to Eq. 15, the time dependency is governed by periodic trigonometric functions. Thus, in the finite system, if the response dynamics is accurate for the largest period of oscillations $t > \frac{2\pi}{\Delta_{JI} \pm \omega}$ (or for the smallest $\Delta_{JI} \pm \omega$ excluding resonance), it remains accurate for any simulation time. As system size increases, the longest oscillation periods grow, making it increasingly challenging for second-order response to reproduce exact dynamics at long

times.

Remarkably, we have additionally verified that even up to 20 sites, no deviation is seen between the linear (left of Fig. 3) or quadratic and linear (middle of Fig. 3) response and exact time propagation at the most distant sites from the absorber for the considered perturbations. This is again explained by the fact that, for the particular localised spatial perturbation the higher orders do not add new possibilities to transport charge (see analyses in Section 2.3).

The right panel of Fig. 3 shows the Fourier transform of the dipole within the absorber (orange) and in the electron transport layer (blue) for a delta-kick perturbation, applied locally in the absorber. This perturbation allows us to see the full spectrum of excitations. The lowest energy peak corresponds to the energy difference between excited states, which corresponds to the second order contribution. It illustrates how second-order effects dominate away from the absorber region. While linear response accurately captures coherent dynamics at the perturbation site, relevant for optical absorption, second-order contributions become dominant farther out at electron/hole transport layers, enabling charge transport (see middle panel of Fig. 3). This aligns with Fig. 1, which shows that second-order matrix elements allow for charge propagation away from the perturbation.

4.2 Current vs. charge dynamics

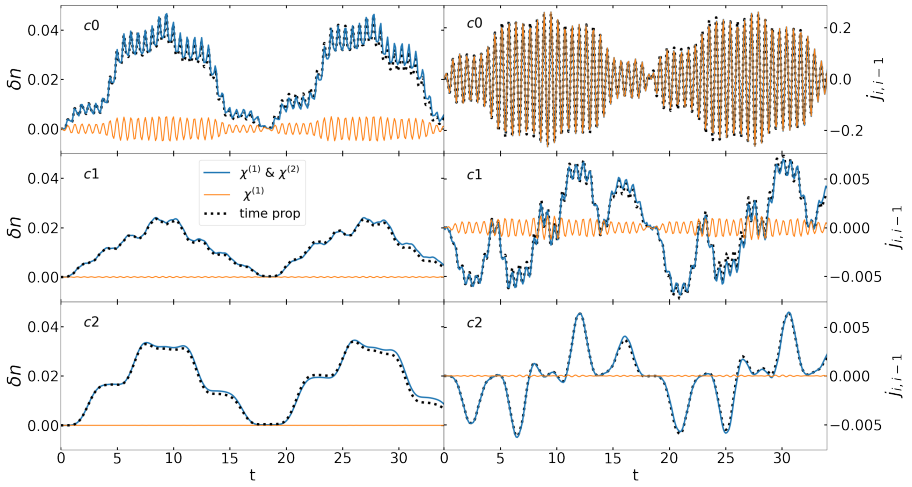

Figure 4: Model with 3 valence and 3 conduction sites with an oscillating external perturbation $0.01 t_h \sin(\omega t)$ for non-resonant ω. Exact time propagation (black) and the response theory (blue) and only from the linear response (orange). Left: Occupation of 3 conduction sites (top to bottom: c0, c1 and c2). Right: The current between the two sites (v0-c0, c0-c1 and c1-c2).

We will now compare the current density evaluated in linear Eq. 11 and quadratic Eqs. 18-19 response to an exact time-dependent current density evaluated with Eq. 2. The same current can be obtained from the continuity equation, $\frac{\partial \rho(\mathbf{r},t)}{\partial t} = -\nabla \cdot \mathbf{j}(\mathbf{r},t)$, which is valid order-by-order.

Fig. 4 shows the density (left panels) and current (right panels) for three conduction sites. The perturbation is oscillating with a non-resonant frequency, the amplitude is such that a slight deviation between the second order response and time propagation can be seen. The advantage of the response theory is that it is possible to separate oscillating linear response (orange lines in Fig. 4) from a less oscillating (with a large period of oscillation) second order. This can be useful during the analysis and for a potential comparison to experimentally measured current. In the absorber region $c0$, where the linear response contribution is similar in

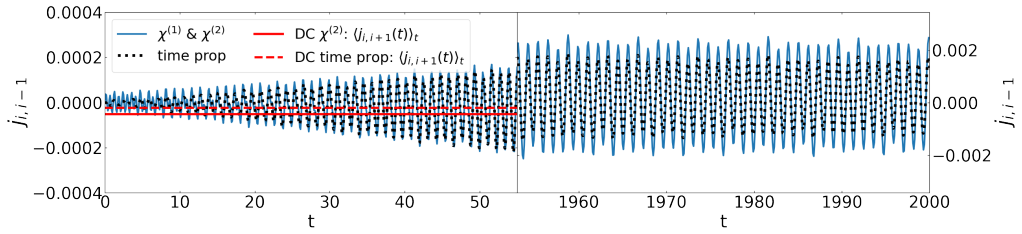

Figure 5: Same model as Fig. 4. Current at resonance frequency at the last site of electron level $c1 - c2$ evaluated in response theory (blue) and in exact time propagation (black). Left: beginning of the dynamics, where the time propagation and second order response agree. Right: later part of the dynamics, where the response starts to diverge. Red lines are the average current over the full time interval (DC component) from second order response (solid) and from time dynamics (dashed). Note that the scale is different between the two panels.

magnitude to the second-order term, the current, primarily capturing charge oscillations, can be well approximated by the linear response. This is not true for the density itself, so clearly, the validity range of the linear response current extends further than that of the linear response charge density. The current, which is proportional to the time derivative of the charge density, is more sensitive to the oscillations of the density rather then to its overalls shifts. Moreover, the current operator is more delocalized than the density operator, which also results in an extended validity of the linear response current. Fig. 4 also demonstrates the conclusions of section 2.3: for a localised perturbation, in the linear response one can only propagate charge in the vicinity of the perturbation and close to the ground state. In the second order, where the overlaps between the excited states are present, charge can be propagated much further.

Figure 5 shows the current at resonance in response theory and in exact propagation. The left panel shows the beginning of the simulation (up to $60t_h$), as in the case of charge dynamics, the two approaches, exact and response, agree (except some oscillations in the beginning that are due to the resonance). Even at the end of the simulation the difference between the response theory current and the exact one is not dramatic (right panel of Fig. 5). However, the charge dynamics obtained from response theory deviates from the exact propagation and diverges rapidly (see blue lines in the upper left panel of Fig. 6), leading to an unphysical total occupation. While the timescale of divergence differs in smaller systems, we have verified that the conclusion holds for the system considered here. The good behavior of the current can be seen by computing the average current (red lines of Fig. 5), also being a DC component of current density or shift current (for this model) can only be obtained at resonance, as can be seen from Eqs. 18 and 19. Up to $\sim 1000t_h$ two DC components (from second order and from time propagation) agree, after that the second order DC component starts to diverge from the exact one, and it will continue to diverge due to the presence of a linear in time term in the expression Eq. 18.

4.3 Second order: limits and analyses

Here the limits of quadratic response theory in terms of perturbation frequency and amplitude will be examined. Here and in the next sections only charge density dynamics will be discussed. First, in Fig. 6 (top left panel), keeping the perturbation amplitude fixed at $I = 0.1t_h$ we vary the frequency from the near resonant (blue lines) to a non-resonant (orange line). Out-of-resonance the response aligns with the exact dynamics (green line). Approaching the resonance, the denominator in the second order equations Eqs. 15-17 approaches zero, making the response theory non-convergent (blue and orange dashed lines). In the exact time propagation (solid lines) in the resonance ($\Delta_{IJ} = \omega$) the response can be fitted to

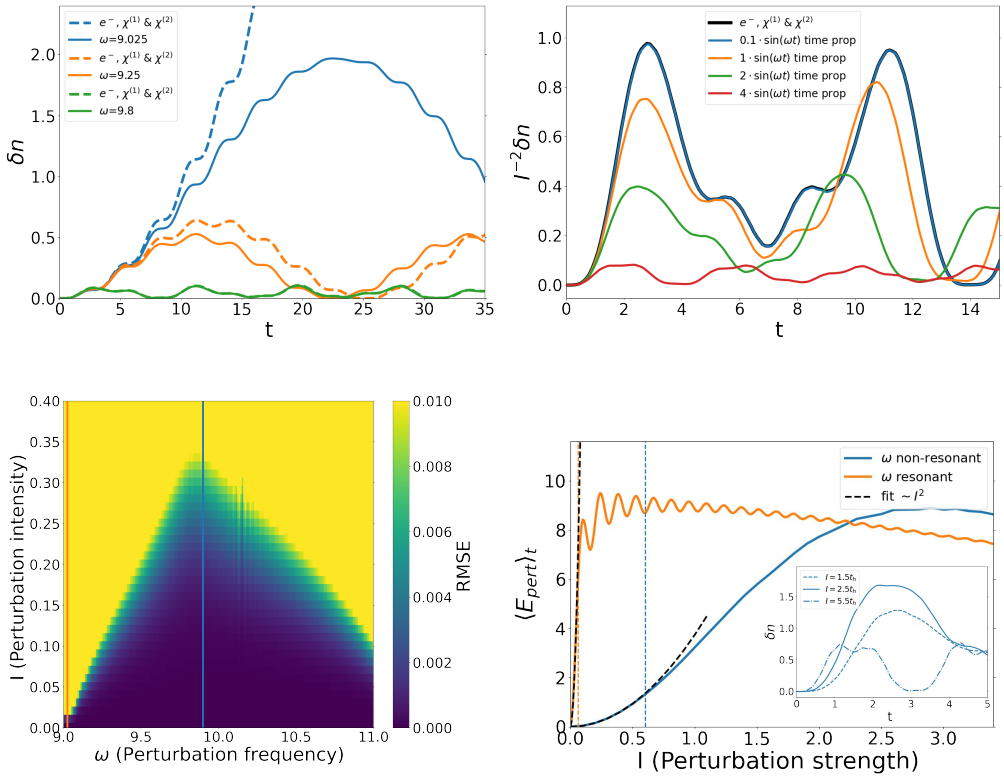

Figure 6: On the top panels we are following occupation of the electron transport layer. The hopping between the conduction and valence sites is $t_a = 0$, which makes the linear response to vanish. The perturbation is $e(t) = I\sin(\omega t)$. Top left: Quadratic response and exact time propagation for different perturbation frequencies ω. Top right: Black solid line result obtained using $\chi^{(2)}$, colored lines correspond to exact time propagation $I^{-2}\cdot n^{RT}(t)$. Bottom left: Root mean squared error map of the induced density in the electron transport layer obtained up to quadratic response as a function of perturbation frequency ω and amplitude I (in the units of t_h). Bottom right: Average energy received by the system over a fixed simulation time as a function of perturbation strength obtained from exact time propagation for resonant (orange) and non-resonant (blue) frequencies. Black dashed lines are quadratic fits. Blue and orange dashed vertical lines correspond to the validity range of the quadratic fit. The inset (obtained with exact time propagation) shows the exact charge density at electron layer for a non-resonant perturbation at three different intensities.

cos$[(\Delta_{IJ} \pm \omega_{eff})t]/(\Delta_{IJ} \pm \omega_{eff})$ with an effective frequency $\omega_{eff} < \omega$. The role of higher orders is to introduce such more fluctuating terms.

Turning to the variations of perturbation amplitude, a fixed off-resonant frequency is considered. As shown in Fig. 6 (top right panel), the quadratic response remains accurate up to $I = 0.3t_h$. Beyond this threshold, higher-order effects become visible: the amplitude of charge oscillations decreases, and additional high-frequency components appear. The bottom left panel of Fig. 6 shows the root mean squared error (RMSE) as a function of external perturbation amplitude and frequency. Using a threshold RMSE of 0.01, the second-order response is valid for $I \lesssim 0.01t_h$ near resonance (orange line) and up to $I \sim 0.3t_h$ in the off-resonant regime (blue line). From the overall trends in the upper panels and in the bottom left panel of Fig. 6, a convergence parameter for the validity of the response theory becomes evident: $I/\Delta_{IJ} \pm \omega < 1$ that was already discussed at the end of section 2.2.2. Approaching the resonance, the valid perturbation amplitude is decreasing proportionally. This condition delineates the regime where the perturbative expansion converges and second-order theory is quantitatively reliable.

Next, we investigate the amount of energy transferred to the system for a fixed period of time as a function of the perturbation amplitude, defined as:

$$\langle E_{pert}\rangle_T = \frac{1}{T}\int_T dt\langle\Psi(t)|\hat{H}|\Psi(t)\rangle - E_0. \tag{24}$$

The bottom right panel of Fig. 6 illustrates this quantity, computed in exact time propagation, for a resonant (orange) and non-resonant (blue) frequency. Characteristic energy behaviour for a linear regime is when the energy delivered to the system by an external field is proportional to the square of its amplitude, $E_{\text{pert}} \propto I^2$, [28]. The figure shows that this holds up to $I \approx 0.6t_h$ for a non-resonant and up to $I \approx 0.1t_h$ for a resonant frequency. Above this values higher-order effects emerge. These thresholds exceed the intensities where deviations in second-order charge density from exact dynamics become visually apparent (see Fig. 6, bottom left; orange for resonant, blue for non-resonant cases). This indicates that the energy transferred into the system is still within the linear regime, when the deviations in the second order response appear. The inset of Fig. 6 (bottom right) shows the charge density at electron layer for a non-resonant perturbation for three intensities, before the energy saturation (dashed), at the maximum of energy (solid) and after the maximum (dashed-dotted). The saturation in energy is reached, when the induced charge density reaches its maximum. Beyond the saturation, the induced charge density decreases, resulting in the decrease of average energy.

4.4 Second order: approximations

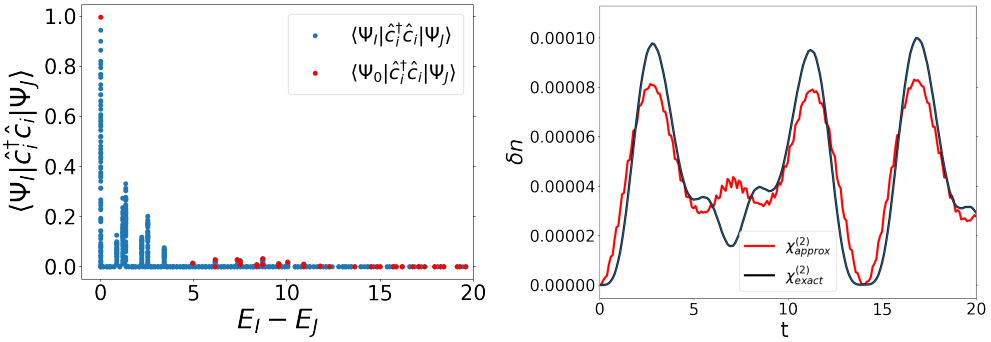

Figure 7: Left: matrix element $\langle\Psi_I|\hat{c}_i^\dagger\hat{c}_i|\Psi_J\rangle$ computed on the last electron site of the system of 4 valence and 4 conduction sites (far from the perturbation) as a function of energy difference $E_J - E_I$. In red only the contributions between the ground and excited states are selected. Right: An approximation to the second order, consisting in keeping only the diagonal elements of the density matrix or, equivalently, only the first line of Eq. 13.

Calculating the second-order response function is computationally demanding, so approximations are necessary. Its structure is analyzed here and feasible approximations are recommended. Firstly, spatial and temporal integrals should be handled in advance, either analytically for temporal perturbations (as in this work) or numerically for spatial perturbations when modeling real materials. It will help to avoid the calculation of the entire response function, limiting it to the elements that couple to the external perturbation.

A primary bottleneck in calculating second order response is the summation over excited states (Eq. 13). Note that here the matrix elements with the ground state (red points in Fig. 7 left) are small compared to the matrix elements between different excited states. The matrix elements with the ground state are present in the linear response Eq. 8 and in the last term of the second order Eq. 13 via $O_{0I}(\mathbf{r})$. These linear-response-like terms are then neglected without any effect on the results. This approximation reduces drastically the amount of computation,

now one only needs to compute the wings of the spatial integral with the perturbation $\tilde{V}_{0J}$. The matrix elements entering the second term of Eq. 13, $\langle\Psi_I|\hat{c}_i^\dagger\hat{c}_i|\Psi_J\rangle$ tend to vanish for energetically distant states, supporting the introduction of a cutoff (here is at $E_I - E_J \sim 11t$ see Fig. 7 left). Left panel of Fig. 7 also confirms the importance of the first term in Eq. 13, since the biggest contribution comes from the diagonal matrix elements.

An important approximation is obtained by only keeping the first line in Eq. 13, which means expanding the time-dependent wave functions on both sides of Eq. 2 only up to the first order. Only diagonal elements of the density matrix of Eq. 2 are introduced, which should capture the non-coherent processes and result in charge transport and separation. The quality of this approximation can be seen in Fig. 7 (right). Indeed, it qualitatively captures the second order response, this has been verified for a large range of perturbation intensities and frequencies. The CPU time for this approximation scales as the linear response one with system size (see Appendix B). Moreover, as discussed earlier, all the ingredients can be obtained within the linear response TDDFT.

4.5 Interaction

Finally, it is interesting to explore whether the Coulomb interaction changes the validity of linear and quadratic response. The interaction primarily modifies the eigenenergies, lifting some degeneracies, but can also modify the eigenfunctions. Onsite interaction can result in the suppression of the charge dynamics, as it was demonstrated in Ref. [49,50] for the Hubbard model. It can also create new spatial pathways for charge dynamics in molecules, which was shown in Ref. [51] by *ab-initio* simulations.

Here, the effect of onsite interaction $+U\sum_i \hat{n}_{i\downarrow}\hat{n}_{i\uparrow}$ for an instantaneous delta-kick perturbation is examined. The spin is introduced, doubling the number of electrons to $N_e = 2(N+1)$. The response and the exact time propagation are computed from the many-body states. In the current model, Fig. 8 (upper panel), which shows the electron layer occupation, one can observe a general reduction by an order of magnitude of the charge density flow by increasing the interaction, as in Ref. [49]. In general, the interaction can change the eigenvalues, which may bring the system in or out of resonance with an oscillating perturbation of a given frequency. This would drastically change the charge separation.

One of the effects of the interaction is altering the ground state, strong interaction prevents the double occupancy of sites (blue, $U = 5$, vs purple, $U = 50$, bars, lower right panel of Fig. 8), which modifies the validity range of response theory. Based on the overlap interpretation (Fig. 1), a more extended ground state results in a more accurate linear response. Indeed, in the strong-interaction regime (right panel), where the ground state is delocalized over all sites, linear response dominates. In contrast, for weak interactions, the ground state remains localized on valence sites, enhancing the second-order response in the transport layer. However, as the linear response stays oscillating around zero, the charge separation is suppressed with the onsite interaction U.

To assess the role of Coulomb repulsion beyond the on-site term, we include a nearest-neighbour interaction $+V\sum_i \hat{n}_i\hat{n}_{i+1}$ with $\hat{n}_i = \hat{n}_{i\downarrow} + \hat{n}_{i\uparrow}$, at fixed $U = 5$. In the extended Hubbard model this term mimics the shortest-range component of long-range interactions [52] and has been argued to be essential for excitonic effects [50, 53]. The lower-left panel of Fig. 8 shows how varying V affects the charge dynamics at $U = 5$: for moderate $V < U$ the dynamics is enhanced relative to the $V = 0$ case (compare green line of lower left panel to blue line of upper left panel of Fig. 8), whereas for larger V it is suppressed, in agreement with Ref. [50]. Our additional observation is that the second-order response decreases as V increases (compare dotted, only linear response, and solid lines in the lower-left panel of Fig. 8). The underlying mechanism differs from the purely on-site case: already in the ground state the local occupation pattern shifts weight toward the higher-energy sites $c1$ (red bars, lower-right panel of

Fig. 8), favouring bound electron-hole configurations and thus blocking spatial charge separation. This is coherent with the conclusion of Ref. [50] about the increased excitonic effects for increased V. A full analysis of interaction-driven excitonic effects on charge dynamics and separation is beyond the scope of this work.

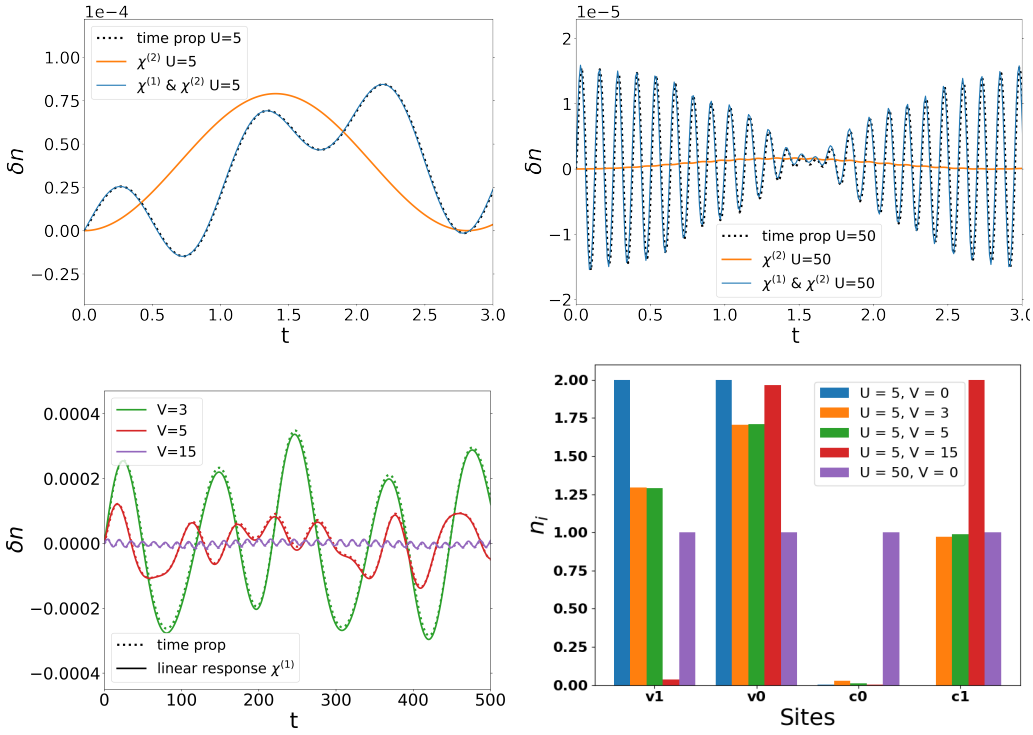

Figure 8: Effect of the interaction on charge dynamics. The perturbation is $e(t) = 0.1t_h \cdot \delta(t)$. Upper left: onsite moderate interaction $U = 5$. Upper right: onsite strong interaction $U = 50$. Lower left: onsite interaction $U = 5$ and varying nearest-neighbour interaction V. Lower right: site occupations $n_i = \langle \hat{n}_{i\uparrow} + \hat{n}_{i\downarrow} \rangle$ of the ground state for varying onsite U and nearest-neighbour V interactions

5 Conclusions

Time propagation of a wave function for a system under perturbation allows one to access the time evolution of all observables. In this article we have focused on the charge dynamics, charge separation, current and energy transfer under various weak perturbations, pertinent to optoelectronic and photovoltaic applications. We have explored and benchmarked a response theory framework to compute these quantities. Using a numerically solvable site model, we demonstrated that linear response accurately describes coherent charge oscillations under weak perturbations but fails to capture any net charge separation. In contrast, quadratic response theory includes off-diagonal density matrix contributions that enable asymmetric charge propagation and net transport, providing excellent agreement with exact time propagation over a broad range of conditions.

We identified a clear criterion for the validity of second-order response: the amplitude-to-resonance ratio $I/(\Delta_{IJ} \pm \omega) < 1$. This sets the boundary where perturbative approaches remain reliable, with broader validity in non-resonant regimes. We introduced practical approximation to the second order response, that only requires quantities that can be obtained within the linear response TDDFT, which drastically reduces computational demands with minimal

loss of accuracy. Second-order response also correctly captures DC components in the current (shift currents), absent in linear response, and remains robust even as density dynamics begin to diverge. Notably, we find that strong on-site and nearest-neighbour interactions extend the range of linear response applicability by delocalizing the ground state.

These results highlight the predictive power of the response theory up to the second order. They also show that with respect to long-time propagation the response theory may be more efficient with respect to full time propagation. While its formal scaling is worse - due to the double sum over states - response functions need only be computed once and allow access to all time scales and perturbations. In practice, symmetries, cutoffs, and proposed controlled approximations significantly reduce computational cost. We expect the response theory to hold for weak perturbations when exploring realistic systems with interfaces and interactions such as electron–hole or electron–phonon coupling.

This work highlights the possibility of response theory for accurately simulating spatially resolved charge dynamics in systems influenced by varying external perturbations, making it a valuable tool for studying fundamental questions and for contributing to the technological advancement in photovoltaic and optoelectronic applications.

Acknowledgements

We thank Matteo Gatti and Valérie Veniard for useful discussions.

Author contributions L.L., L.R., and V.G. conceived the project and explored the theoretical framework. L.L. and V.G. implemented the simulation code. V.G. carried out the simulations and data analysis. All authors discussed the results and contributed to writing the manuscript.

Funding information This work benefited from the support of EDF in the framework of the research and teaching Chair "Sustainable energies" at Ecole Polytechnique (V.G.) and from the European Union's Horizon 2020 research and innovation programm under the Marie Sklodowska-Curie grant agreement No. 101030447 (L.L.).

A Changing perturbation extension

Figure 9 (left panel) shows the effect of a delocalized external perturbation $\hat{V}^{IJ}_{ext}(t) = I\delta_{ji+1}(\hat{c}^\dagger_i\hat{c}_i + \hat{c}^\dagger_i\hat{c}_{i+1} + \hat{c}^\dagger_{i+1}\hat{c}_i)e(t)$ on the dynamics of an occupation at electron layer $c1$ under strong driving ($I = 0.3t_h$), where second order start to break down. For a localized perturbation (orange), only the absorber region is perturbed, as throughout this work. In contrast, a fully delocalized perturbation (green) acts on all sites. The difference arises from additional matrix elements $\tilde{V}_{IJ}$ in the third-order response (see Eq. 22) and is a purely third-order effect, becoming relevant at longer propagation time. Right panel of Fig. 9 shows that the response theory (blue line) cannot capture the differences between the delocalized perturbation and localized one obtained in exact time propagation (black line). This means that the delocalized perturbation can shift the regime, where the second order is valid into weaker perturbations.

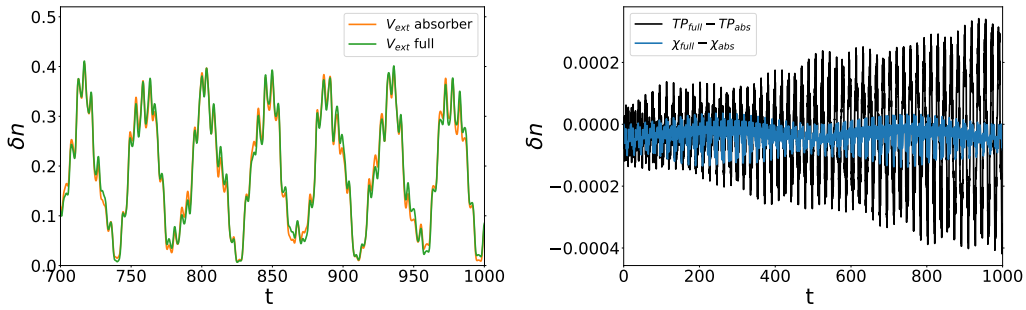

Figure 9: The effect of a localised (on absorber) and delocalised perturbation on charge dynamics of the occupation of the last site on the electron transport layer. The perturbation amplitude is $0.3t_h$, where the third order starts to become important. Left: computed in exact time propagation (TP) under extended perturbation (green) and localized on the absorber (orange). Right: differences between TP under extended and localized perturbations (black) and the same difference in the response theory (blue).

B Scaling with system size

Figure 10 shows CPU time scaling with system size. For exact time propagation (blue), each time step involves a full diagonalization, scaling as $\mathcal{O}(N^3)$ with Hilbert space size N. Linear response (orange) requires matrix-vector products and a single sum over states, also scaling as $\mathcal{O}(N^3)$. Quadratic response (green) involves a double sum, leading to $\mathcal{O}(N^4)$ scaling. The approximate second-order scheme from Sec. 4.4 reduces this to $\mathcal{O}(N^3)$ (red). The the full second-order computation time can be reduced in practice by considering cutoffs in the summations and using symmetries. Moreover, the response functions are naturally parallelizable. Instead, time propagation cost is rather a lower limit, since it requires a certain number of time steps and a time-step size convergence study. Importantly, unlike time propagation, once computed, response functions give access to all time scales and allow changes in external perturbations without redoing the full calculation.

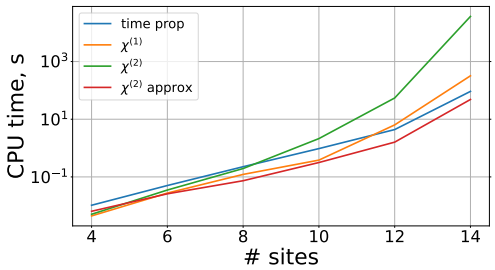

Figure 10: CPU time to compute one step of exact dynamics (blue), full scaling of first ($\chi^{(1)}$) (orange), second ($\chi^{(2)}$) (green) order response and an approximation to second order response ($\chi^{(2)}$ approx) (red) as a function of number of sites. Each calculation is performed on 1 CPU core.

References

[1] C. A. Ullrich, *Time-Dependent Density-Functional Theory: Concepts and Applications*, Oxford University Press, Oxford, ISBN 9780199563029 (2012).

[2] M. A. L. Marques, N. T. Maitra, F. M. S. Nogueira, E. K. U. Gross and A. Rubio, eds.,

Fundamentals of Time-Dependent Density Functional Theory, vol. 837 of *Lecture Notes in Physics*, Springer, Berlin, Heidelberg (2012).

[3] G. Stefanucci and R. Van Leeuwen, *Nonequilibrium many-body theory of quantum systems: A modern introduction*, vol. 9780521766, ISBN 9781139023979, doi:10.1017/CBO9781139023979 (2010).

[4] J. I. Fuks, P. Elliott, A. Rubio and N. T. Maitra, *Dynamics of charge-transfer processes with time-dependent density functional theory*, Journal of Physical Chemistry Letters **4**(5), 735 (2013), doi:10.1021/jz302099f.

[5] P. Schaffhauser and S. Kümmel, *Using time-dependent density functional theory in real time for calculating electronic transport*, Physical Review B **93**(3), 35115 (2016), doi:10.1103/PhysRevB.93.035115.

[6] N. T. Maitra, *Charge transfer in time-dependent density functional theory*, Journal of Physics Condensed Matter **29**(42), 423001 (2017), doi:10.1088/1361-648X/aa836e, 1707.08054.

[7] L. Lacombe and N. T. Maitra, *Non-adiabatic approximations in time-dependent density functional theory: progress and prospects*, npj Computational Materials **9**(1) (2023), doi:10.1038/s41524-023-01061-0, 2302.11366.

[8] S. Kümmel, *Charge-transfer excitations: A challenge for time-dependent density functional theory that has been met*, Advanced Energy Materials **7**(16), 1700440 (2017), doi:https://doi.org/10.1002/aenm.201700440, https://onlinelibrary.wiley.com/doi/pdf/10.1002/aenm.201700440.

[9] D. B. Dar, A. Baranova and N. T. Maitra, *Reformulation of Time-Dependent Density Functional Theory for Nonperturbative Dynamics: The Rabi Oscillation Problem Resolved*, Physical Review Letters **133** (2024), doi:10.1103/PhysRevLett.133.096401.

[10] P. Lipavský, V. Špička and B. Velický, *Generalized kadanoff-baym ansatz for deriving quantum transport equations*, Phys. Rev. B **34**, 6933 (1986), doi:10.1103/PhysRevB.34.6933.

[11] Y. Pavlyukh, E. Perfetto, D. Karlsson, R. van Leeuwen and G. Stefanucci, *Time-linear scaling nonequilibrium green's function methods for real-time simulations of interacting electrons and bosons. i. formalism*, Phys. Rev. B **105**, 125134 (2022), doi:10.1103/PhysRevB.105.125134.

[12] N. E. Dahlen and R. van Leeuwen, *Solving the kadanoff-baym equations for inhomogeneous systems: Application to atoms and molecules*, Phys. Rev. Lett. **98**, 153004 (2007), doi:10.1103/PhysRevLett.98.153004.

[13] C. Attaccalite, M. Grüning and A. Marini, *Real-time approach to the optical properties of solids and nanostructures: Time-dependent Bethe-Salpeter equation*, PHYSICAL REVIEW B **84**, 245110 (2011), doi:10.1103/PhysRevB.84.245110.

[14] S. Latini, E. Perfetto, A.-M. Uimonen, R. van Leeuwen and G. Stefanucci, *Charge dynamics in molecular junctions: Nonequilibrium green's function approach made fast*, Phys. Rev. B **89**, 075306 (2014), doi:10.1103/PhysRevB.89.075306.

[15] P. Miguel, M. C. De Melo and A. Marini, *Unified theory of quantized electrons, phonons, and photons out of equilibrium: A simplified ab initio approach based on the generalized Baym-Kadanoff ansatz*, PHYSICAL REVIEW B **93**, 155102 (2016), doi:10.1103/PhysRevB.93.155102.

[16] Y. Pavlyukh, E. Perfetto and G. Stefanucci, *Photoinduced dynamics of organic molecules using nonequilibrium Green's functions with second-Born, GW, T -matrix, and three-particle correlations PHOTOINDUCED DYNAMICS of ORGANIC MOLECULES ... PAVLYUKH, PERFETTO, and STEFANUCCI*, Physical Review B **104**(3) (2021), doi:10.1103/PhysRevB.104.035124.

[17] Y. Pavlyukh, E. Perfetto, D. Karlsson, R. Van Leeuwen and G. Stefanucci, *Time-linear scaling nonequilibrium Green's function method for real-time simulations of interacting electrons and bosons. II. Dynamics of polarons and doublons*, Physical Review B **105**(12), 1 (2022), doi:10.1103/PhysRevB.105.125135.

[18] R. Tuovinen, Y. Pavlyukh, E. Perfetto and G. Stefanucci, *Time-Linear Quantum Transport Simulations with Correlated Nonequilibrium Green's Functions*, Physical Review Letters **130**(24), 246301 (2023), doi:10.1103/PhysRevLett.130.246301, 2211.15635.

[19] E. Perfetto and G. Stefanucci, *Real-time gw-ehrenfest-fan-migdal method for nonequilibrium 2d materials*, Nano Letters **23**(15), 7029 (2023), doi:10.1021/acs.nanolett.3c01772, PMID: 37493350, https://doi.org/10.1021/acs.nanolett.3c01772.

[20] D. Sangalli, *Excitons and carriers in transient absorption and time-resolved arpes spectroscopy: An ab initio approach*, Phys. Rev. Mater. **5**, 083803 (2021), doi:10.1103/PhysRevMaterials.5.083803.

[21] Y. Pavlyukh, *Nonequilibrium dynamics of the hubbard dimer*, physica status solidi (b) **261**(9), 2300510 (2024), doi:https://doi-org.inc.bib.cnrs.fr/10.1002/pssb.202300510, https://onlinelibrary-wiley-com.inc.bib.cnrs.fr/doi/pdf/10.1002/pssb.202300510.

[22] G. Stefanucci and E. Perfetto, *Excitonic Bloch equations from first principles*, SciPost Phys. **18**, 009 (2025), doi:10.21468/SciPostPhys.18.1.009.

[23] *The 2025 roadmap to ultrafast dynamics: Frontiers of theoretical and computational modelling* (2025), 2501.06752.

[24] C. C. Reeves, G. Harsha, A. Shee, Y. Zhu, T. Blommel, C. Yang, K. B. Whaley, D. Zgid and V. c. v. Vlček, *Performance of wave function and green's function methods for non-equilibrium many-body dynamics*, Phys. Rev. Res. **7**, 023002 (2025), doi:10.1103/PhysRevResearch.7.023002.

[25] R. Kubo, *Statistical-mechanical theory of irreversible processes. i. general theory and simple applications to magnetic and conduction problems*, Journal of the Physical Society of Japan **12**(6), 570 (1957), doi:10.1143/JPSJ.12.570, https://doi.org/10.1143/JPSJ.12.570.

[26] R. W. Boyd, *Nonlinear Optics*, Academic Press, Cambridge, MA, 4th edn., ISBN 9780128110027 (2020).

[27] G. Onida, L. Reining and A. Rubio, *Electronic excitations: density-functional versus many-body green's-function approaches*, Rev. Mod. Phys. **74**, 601 (2002).

[28] H. Hora, *Y. R. Shen, The Principles of Nonlinear Optics, John Wiley; Sons, New York, 1984, 576 pages.*, vol. 4, doi:10.1017/S0263034600001889 (1986).

[29] L. Prussel and V. Véniard, *Linear electro-optic effect in semiconductors: Ab initio description of the electronic contribution*, Physical Review B **97**(20), 205201 (2018), doi:10.1103/PhysRevB.97.205201.

[30] M. Cheng, Z. Z. Zhu and G. Y. Guo, *Strong bulk photovoltaic effect and second-harmonic generation in two-dimensional selenium and tellurium*, Physical Review B **103**(24), 1 (2021), doi:10.1103/PhysRevB.103.245415, 2012.01124.

[31] E. Luppi, H. Hübener and V. Véniard, *Communications: Ab initio second-order nonlinear optics in solids*, Journal of Chemical Physics **132**(24) (2010), doi:10.1063/1.3457671.

[32] E. Luppi, H. Hübener and V. Véniard, *Ab initio second-order nonlinear optics in solids: Second-harmonic generation spectroscopy from time-dependent density-functional theory*, Physical Review B - Condensed Matter and Materials Physics **82**(23), 235201 (2010), doi:10.1103/PhysRevB.82.235201.

[33] H. Hübener, E. Luppi and V. Véniard, *Ab initio calculation of second harmonic generation in solids*, Physica Status Solidi (B) Basic Research **247**(8), 1984 (2010), doi:10.1002/PSSB.200983954.

[34] C. Attaccalite and M. Grüning, *Nonlinear optics from an ab initio approach by means of the dynamical berry phase: Application to second- and third-harmonic generation in semiconductors*, Phys. Rev. B **88**, 235113 (2013), doi:10.1103/PhysRevB.88.235113.

[35] H. Hübener, *Second-order response Bethe-Salpeter equation*, PHYSICAL REVIEW A **83**, 62122 (2011), doi:10.1103/PhysRevA.83.062122.

[36] A. Riefer and W. G. Schmidt, *Solving the bethe-salpeter equation for the second-harmonic generation in zn chalcogenides*, Phys. Rev. B **96**, 235206 (2017), doi:10.1103/PhysRevB.96.235206.

[37] T. Baumgratz, M. Cramer and M. B. Plenio, *Quantifying coherence*, Physical Review Letters **113**(14) (2014), doi:10.1103/PhysRevLett.113.140401, 1311.0275.

[38] A. L. Fetter and J. D. Walecka, *Quantum Theory of Many-Particle Systems*, McGraw-Hill, New York (1971).

[39] P. Cudazzo and L. Reining, *Correlation satellites in optical and loss spectra*, Physical Review Research **2**(1) (2020), doi:10.1103/PhysRevResearch.2.012032.

[40] P. Cudazzo, *First-principles description of the exciton-phonon interaction: A cumulant approach*, Physical Review B **102**(4), 1 (2020), doi:10.1103/PhysRevB.102.045136.

[41] E. Perfetto, Y. Pavlyukh and G. Stefanucci, *Real-time gw: Toward an ab initio description of the ultrafast carrier and exciton dynamics in two-dimensional materials*, Phys. Rev. Lett. **128**, 016801 (2022), doi:10.1103/PhysRevLett.128.016801.

[42] F. Furche and R. Ahlrichs, *Adiabatic time-dependent density functional methods for excited state properties*, The Journal of Chemical Physics **117**(16), 7433 (2002), doi:10.1063/1.1508368, https://pubs.aip.org/aip/jcp/article-pdf/117/16/7433/19317804/7433_1_online.pdf.

[43] E. I. Sánchez-Flores, R. Chávez-Calvillo, T. A. Keith, G. Cuevas, T. Rocha-Rinza and F. Cortés-Guzmán, *Properties of atoms in electronically excited molecules within the formalism of tddft*, Journal of Computational Chemistry **35**(10), 820 (2014), doi:https://doi.org/10.1002/jcc.23559, https://onlinelibrary.wiley.com/doi/pdf/10.1002/jcc.23559.

[44] J. E. Sipe and A. I. Shkrebtii, *Second-order optical response in semiconductors*, Physical Review B **61**, 5337 (2000), doi:10.1103/PhysRevB.61.5337.

[45] S. M. Young and A. M. Rappe, *First-principles calculation of the bulk photovoltaic effect in bismuth ferrite*, Physical Review Letters **109**(11), 116601 (2012), doi:10.1103/PhysRevLett.109.116601.

[46] ASTM International, *Standard tables for reference solar spectral irradiances: Direct normal and hemispherical on 37° tilted surface*, https://www.astm.org/g0173-03r20.html, ASTM G173-03(2020), West Conshohocken, PA (2020).

[47] Y. Zhang, R. Mondaini and R. T. Scalettar, *Photoinduced enhancement of superconductivity in the plaquette hubbard model*, Phys. Rev. B **107**, 064309 (2023), doi:10.1103/PhysRevB.107.064309.

[48] Y. Wang, M. Claassen, B. Moritz and T. P. Devereaux, *Producing coherent excitations in pumped mott antiferromagnetic insulators*, Phys. Rev. B **96**, 235142 (2017), doi:10.1103/PhysRevB.96.235142.

[49] R. Steinigeweg, F. Jin, H. De Raedt, K. Michielsen and J. Gemmer, *Charge diffusion in the one-dimensional hubbard model*, Phys. Rev. E **96**, 020105 (2017), doi:10.1103/PhysRevE.96.020105.

[50] K. A. Al-Hassanieh, F. A. Reboredo, A. E. Feiguin, I. González and E. Dagotto, *Excitons in the one-dimensional hubbard model: A real-time study*, Phys. Rev. Lett. **100**, 166403 (2008), doi:10.1103/PhysRevLett.100.166403.

[51] V. Despré and A. I. Kuleff, *Correlation-driven charge migration as an initial step of the dynamics in correlation bands*, Phys. Rev. A **106**, L021501 (2022), doi:10.1103/PhysRevA.106.L021501.

[52] F. Gebhard, K. Bauerbach and O. Legeza, *Screening in hubbard models with long-range interactions*, Phys. Rev. B **111**, 205146 (2025), doi:10.1103/PhysRevB.111.205146.

[53] E. Jeckelmann, *Optical excitations in a one-dimensional mott insulator*, Phys. Rev. B **67**, 075106 (2003), doi:10.1103/PhysRevB.67.075106.